Solar-driven efficient degradation of emerging contaminants by g-C$_3$N$_4$-shielding polyester fiber/TiO$_2$ composites

Yi Chen, Wangyang Lu*, Haibin Shen, Yan Gu, Tiefeng Xu, Zhexin Zhu, Gangqiang Wang, Wenxing Chen*

National Engineering Lab for Textile Fiber Materials & Processing Technology (Zhejiang), Zhejiang Sci-Tech University, Hangzhou 310018, China

A B S T R A C T

Solar-driven photocatalysis has shown tremendous potential for environmental remediation, but photocatalysts with the strong oxidation ability usually destroy some organic carriers. Herein, we constructed a graphitic carbon nitride (g-C$_3$N$_4$)-shielding polyester fiber (PET)/titanium dioxide (TiO$_2$) composite (g-C$_3$N$_4$-TiO$_2$@LMPET) by using g-C$_3$N$_4$ as an isolation layer to protect the PET from the oxidation damage by hydroxyl radicals (˙OH). The results of photoluminescence and photocurrent indicated that the g-C$_3$N$_4$-TiO$_2$@LMPET has lower photogenerated charge recombination rate. Meanwhile, g-C$_3$N$_4$ broadens the absorption range of the composite to visible region. Therefore, the g-C$_3$N$_4$-TiO$_2$@LMPET composite exhibited a significantly enhanced photocatalytic performance toward the degradation of sulfaquinoxaline (SQX) and thiamethoxam under solar irradiation. Moreover, the g-C$_3$N$_4$-TiO$_2$@LMPET exhibited good repeatability in cyclic experiments. Finally, the possible degradation pathways and mechanisms of SQX and thiamethoxam were proposed. Overall, our work provides a feasible method for constructing efficient and stable photocatalytic materials to eliminating emerging contaminants.

1. Introduction

In recent years, the emerging contaminants, such as antibiotics and pesticides, deriving from animal husbandry and agriculture, have become one of the major sources of surface and groundwater pollution. These contaminants are characterized by long-term toxicity, high resistance to biodegradation, and ease of accumulation in living species, leading to potential threats to the environment and human health [1–4]. In comparison with traditional treatment methods, such as physical adsorption [5,6], biodegradation [7,8], and chemical oxidation [9–11], photocatalysis [12–14] is considered as one of the most promising technologies for wastewater treatment. However, when dispersed in water, most photocatalysts exist in the form of powder, which leads to aggregation during their use and makes them difficult to recycle. To overcome the limitation, many efforts have been made to immobilize the catalyst powders onto some inorganic materials such as silica [15], zeolites [16,17], activated carbon [18,19], glass fiber [20,21], and carbon fiber [22,23]. The main drawbacks of these inorganic supports are that they are not conducive to the loading and recycling of catalysts, and the black carbon fiber materials can reduce the light absorption of photocatalysts. Therefore, organic materials are

regarded as more potential alternatives as sustainable catalyst supports, owing to their flexibility, toughness, and high processability [24–28].

On the other hand, some studies have reported that polymers can be photodegraded in the presence of some photocatalysts [29–31]. These photocatalysts are excited by light to generate powerful oxidizing species (e.g. hydroxyl radicals (˙OH)), which are highly destructive to the structure of polymers. For example, the conventional photocatalyst titanium dioxide (TiO$_2$) has good catalytic activity, but it generates strong oxidizing ˙OH radicals that can damage the organic supports. Besides, its development is hindered because it only absorbs ultraviolet light, which accounts for only about 5% of the total solar energy [32,33]. In addition, TiO$_2$ nanoparticles are prone to be partially coated by carriers or adhesives during the catalyst loading owing to their small particle size, resulting in the reduction of the surface active sites, which directly decreases its photocatalytic performance.

Recently, graphitic carbon nitride (g-C$_3$N$_4$), as a nonmetal polymeric photocatalyst with the advantages of non-toxicity, low cost, visible-light response and good chemical stability, has received extensive attention in organic pollutant degradation [34,35] and energy conversion [36,37]. Moreover, g-C$_3$N$_4$, as a two-dimensional sheet material, can be more easily loaded on the surface of some carriers.
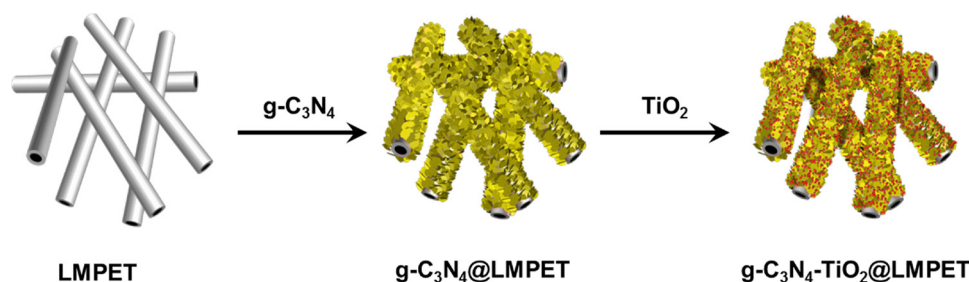
Scheme 1. Schematic diagram of the preparation process of the g-C_3N_4-TiO_2@LMPET composite.

Nevertheless, its photocatalytic activity is limited due to low electron mobility and high recombination rate of the photogenerated electron-hole pairs. As is well known, a wide light absorption range, the suppression of charge recombination, and a high number of active sites are three key factors for high photocatalytic efficiency [38–41], but it is always difficult for a single photocatalyst to meet all three requirements simultaneously. Therefore, significant attempts have been made to optimize the catalytic performance of photocatalysts, including doping [42–44], noble metal deposition [45,46], combination with other catalysts [47–49], and loading on carriers [50].

In this work, our goal is to solve the photo-etching of organic carriers while achieving the improved catalytic performance of photocatalysts. Polyester fiber (PET) was chosen as the appropriate support due to its large availability, light weight and good chemical stability [51,52] compared to other polymers. The two-dimensional g-C_3N_4 sheets were used to coat the surface of PET to construct a g-C_3N_4-shielding PET/TiO_2 composite (g-C_3N_4-TiO_2@LMPET). In the composite, TiO2 plays a major role in the formation of hydroxyl radicals (·OH), and the g-C_3N_4 layer acts as a barrier between the PET support and TiO_2 nanoparticles to protect the PET from the etching by ·OH. Compared with the TiO_2@LMPET and g-C_3N_4@LMPET, the g-C_3N_4-TiO_2@LMPET displayed an obviously enhanced photocatalytic efficiency, which was attributed to the following reasons: (i) the electron transfer between g-C_3N_4 and TiO_2 suppresses the photogenerated charge recombination; (ii) g-C_3N_4 extends the visible light absorption range of the composite; (iii) the g-C_3N_4 layer avoids the wrapping of TiO_2 by fibers and helps to the exposure of active sites. The high photocatalytic activity of g-C_3N_4-TiO_2@LMPET was demonstrated by the degradation of sulfaquinoxaline (SQX) and thiamethoxam under solar irradiation. Recycling tests were carried out to assess the recyclability of g-C_3N_4-TiO_2@LMPET. Furthermore, the stability of the PET support in the composite was estimated. Finally, the possible mechanisms and pathways of degradation were proposed.

2. Experimental

2.1. Materials and reagents

Urea, potassium iodide (KI), isopropyl alcohol (IPA), p-benzoquinone (BQ) and tertiary butanol (TBA) were purchased from Aladdin Reagent Co., China. Titanium dioxide (TiO_2, P25) was provided by Acros Organics, Belgium. Sulfaquinoxaline sodium (SQX) was purchased from Sigma Aldrich Shanghai Trading Co., China. Thiamethoxam and 5,5-dimethyl-1-pyrroline-*N*-oxide (DMPO) were purchased from J&K Chemical Co., China. Dihydroxyethyl terephthalate (BHET) was purchased from Shanghai Maclean Biochemical Technology Co., China. Low-melting polyester fibers (LMPET) were obtained from Huvis Co., South Korea.

2.2. Catalyst preparation

2.2.1. Preparation of g-C_3N_4@LMPET and TiO_2@LMPET

The g-C_3N_4 sheets were synthesized according to a procedure

previously reported in the literature [53]. Typically, 50 g of urea was placed in a crucible and calcined at 550 °C for 3 h under air atmosphere at a heating rate of 2.5 °C/min. A uniform g-C_3N_4 suspension was obtained by ultrasonically dispersing g-C_3N_4 sheets in an ethanol-water (1:1) solution. Next, the non-woven LMPET was immersed in the g-C_3N_4 suspension and then processed by a padding machine (the pressure between the two rollers was 0.2 MPa, the speed of the rollers was 20 rpm). After that, the obtained LMPET supported with g-C_3N_4 was placed in an oven at 80 °C to remove moisture from the LMPET fiber and was then baked at 135 °C to melt the LMPET sheath to strongly stick g-C_3N_4 (the melting temperature of the LMPET sheath was obtained from Fig. S1). Finally, the prepared g-C_3N_4-coated LMPET (g-C_3N_4@LMPET) was washed several times with water to remove the unadhered g-C_3N_4 from the LMPET surface and dried at 60 °C. For comparison purpose, TiO_2-supported LMPET (TiO_2@LMPET) was fabricated using the same preparation procedure as described above.

2.2.2. Preparation of g-C_3N_4-TiO_2@LMPET

g-C_3N_4-TiO_2@LMPET was obtained by the one-step hydrothermal reaction between the above-prepared g-C_3N_4@LMPET and TiO_2 nanoparticles. Prior to the hydrothermal reaction, the g-C_3N_4@LMPET was immersed in the prepared TiO_2 suspension and sonicated. It was then transferred into a Teflon-lined autoclave and maintained at 120 °C for 2 h to achieve the deposition of TiO_2 on the g-C_3N_4@LMPET surface. The final g-C_3N_4-TiO_2@LMPET composite was obtained by washing and drying. The preparation process of the g-C_3N_4-TiO_2@LMPET composite was shown in Scheme 1.

2.3. Characterization

The morphology of the samples was observed by an ULTRA-55 field emission scanning electronic microscopy (FE-SEM). X-ray photoelectron spectra were recorded on a Thermo ESCALAB 250XI X-ray photoelectron spectrometer (XPS). X-ray diffraction (XRD) measurements were performed on a DX-2700 X-ray diffractometer with Cu-Kα radiation. UV–vis diffuse reflection spectra (DRS) were obtained by an UV–vis spectrophotometer (Lambda 900) in the range of 200–800 nm. Fourier-transform infrared spectroscopy (FT-IR) spectra were recorded on a Thermo Nicolet 5700 spectrometer in the range of 600–4000 nm. Raman spectra were obtained on an inVia Qontor spectrometer with an excitation wavelength of 532 nm. Differential scanning calorimetry (DSC) was conducted on a DSC1 (Mettler-Toledo) from 25 to 300 °C with a heating rate of 10 °C/min under air flow. Thermogravimetric analyses (TGA) were carried out on a TGA 1 (Mettler-Toledo) from 25 to 800 °C with a heating rate of 10 °C/min in air atmosphere. Photoluminescence (PL) spectra (excitation wavelength = 345 nm) were recorded on an F-46001 spectrometer (Hitachi, Japan). The contents of C, H, and N were measured by organic elemental analysis (Elementar, Germany). The Ti content was measured by a PerkinElmer NexION 300X inductively coupled plasma-mass spectrometer (ICP-MS). The photocurrent response was performed on an electrochemical workstation (CHI670E, China) using a three-electrode cell system with Pt wire as the counter electrode and Ag/AgCl as reference electrode in

Na$_2$SO$_4$ solution (1 M). The light source was a 100 W lamp (LOToriel GmbH & Co. KG).

2.4. Photocatalytic experiments

The photocatalytic activity of samples was investigated by the degradation experiments of SQX and thiamethoxam in a Q-Sun Xe-1 test chamber (USA). The spectra power distribution (SPD) of Q-Sun Xe-1 with daylight was displayed in Fig. S2. The experiments were conducted in a 40-mL glass bottle, in which a piece of flexible photocatalytic PET fiber mat (130 mg) floated in SQX or thiamethoxam aqueous solution (30 mL, 2×10^{-5} mol/L). The pH of the reaction solution was adjusted by adding H$_2$SO$_4$ or NaOH. At specific intervals of time, the solution was continuously withdrawn and filtered, and the substrate concentration was detected by Ultra-Performance Liquid Chromatography (UPLC, Waters).

2.5. PET support stability experiments

The stability of the PET support was estimated by the degradation experiments of BHET with TiO$_2$ and g-C$_3$N$_4$ under solar irradiation as well as ultraviolet light exposure tests. A small amount of BHET was fully dissolved in ultrapure water to obtain a BHET aqueous solution (2×10^{-5} mol/L). At the same time, the UV light exposure tests of TiO$_2$@LMPET, g-C$_3$N$_4$@LMPET, and g-C$_3$N$_4$-TiO$_2$@LMPET were performed. The UV irradiation parameters were: 400 W of UV lamp power, 365 nm of wavelength, 18 cm of illumination distance, 14 h of illumination time.

3. Results and discussion

3.1. Catalyst characterization

The morphologies of the samples were observed by SEM, as shown in Fig. 1. The pristine LMPET fiber showed a smooth surface, while the surface of the TiO$_2$@LMPET was relatively rough, with small spots due to the immobilization of the TiO$_2$ particles. As is clearly seen from Fig. 1f, the surface of the fibers was covered by a layer of fish scale-like lobes, which suggests that the g-C$_3$N$_4$ sheets had adhered to the surface of LMPET to form a continuous coating. In comparison with the g-C$_3$N$_4$@LMPET, the surface of g-C$_3$N$_4$-TiO$_2$@LMPET became blurrier and rougher, and some TiO$_2$ particle aggregates were observed in the high magnification SEM images, indicating that the TiO$_2$ particles had successfully attached onto the surface of the g-C$_3$N$_4$-coated LMPET. In addition, the successful preparation of g-C$_3$N$_4$-TiO$_2$@LMPET was further confirmed by the mapping analysis. As shown in Fig. 2, C, O, N, and Ti were uniformly distributed on the surface of g-C$_3$N$_4$-TiO$_2$@LMPET. The presence of C and O was assigned to the functional groups of PET. The presence of N and Ti indicated that g-C$_3$N$_4$ and TiO$_2$, were supported onto the LMPET fibers. The N content in the g-C$_3$N$_4$-TiO$_2$@LMPET was determined by organic elemental analysis (Table S1), and the content of g-C$_3$N$_4$ immobilized on the LMPET was calculated to be 3.15 mg. Meanwhile, the Ti content in the g-C$_3$N$_4$-TiO$_2$@LMPET was measured by ICP-MS (Fig. S3 and Table S2), and the content of TiO$_2$ was found to be 3.13 mg XPS analyses were performed to determine the elemental compositions and chemical states of the samples. The surface elemental compositions of LMPET, g-C$_3$N$_4$@LMPET, TiO$_2$@LMPET and g-C$_3$N$_4$-TiO$_2$@LMPET were shown in Fig. 3a. As can be seen from Fig. 3a, C, O, N, and Ti were the main elements detected on the surface of g-C$_3$N$_4$-TiO$_2$@LMPET. Fig. 3b illustrates the high-resolution C 1s spectra. For pristine LMPET, three peaks were observed at 285.0, 286.6, and 289.0 eV, which were attributed to the C−C$_6$H$_4$, O−(CH$_2$)$_2$, and C═O−C bonds in the PET structure, respectively. For the g-C$_3$N$_4$-TiO$_2$@LMPET, another signal at 288.0 eV was detected, related to the N═C−N coordination of g-C$_3$N$_4$ [54,55]. The high-resolution O 1s spectra of LMPET and g-C$_3$N$_4$-TiO$_2$@LMPET are shown in Fig. 3c. The

two peaks located at 532.2 and 533.3 eV were from the O−C═O and C−O bonds, whereas two new peaks at 529.5 and 531.8 eV appeared in the g-C$_3$N$_4$-TiO$_2$@LMPET. The peak at 529.5 eV could be attributed to the Ti-O bond in TiO$_2$ [56,57], while the peak at 531.8 eV could be attributed to the O carried on the s urface of g-C$_3$N$_4$, which also appeared in the O 1s spectrum of g-C$_3$N$_4$ (Fig. S4). Furthermore, considering that the g-C$_3$N$_4$ was prepared in an air atmosphere, the peak at 531.8 eV was attributed to the formation of oxides on the surface of g-C$_3$N$_4$ during the calcination preparation. The results shown in Fig. 3b and c confirmed that g-C$_3$N$_4$ and TiO$_2$ were successfully supported onto the surface of LMPET. The high-resolution C 1s and O 1s spectra of TiO$_2$@LMPET and g-C$_3$N$_4$@LMPET were shown in Fig. S5. As shown in the high-resolution N 1s spectra (Fig. 3d), the spectrum of g-C$_3$N$_4$@LMPET could be divided into three peaks, which were assigned to C═N−C (398.4 eV), N−(C)$_3$ (399.7 eV), and C−N−H (400.9 eV) [58–60]. However, compared to the g-C$_3$N$_4$@LMPET, the characteristic peaks of N 1s in g-C$_3$N$_4$-TiO$_2$@LMPET were slightly shifted towards a higher binding energy and the half-width of peaks at 399.8 and 401.0 eV increased noticeably, revealing that the chemical environment changed due to the interaction between g-C$_3$N$_4$ and TiO$_2$. The Ti 2p spectrum of TiO$_2$@LMPET, shown in Fig. 3e, presented two peaks at 459.0 (Ti 2p$_{3/2}$) and 464.5 eV (Ti 2p$_{1/2}$), whereas the two peaks of g-C$_3$N$_4$-TiO$_2$@LMPET shifted 0.7 and 0.5 eV towards the lower binding energy, respectively [61]. The shift can be ascribed to the effects of electron transfer from g-C$_3$N$_4$ to TiO$_2$ [62]. Based on the above analysis, it can be deduced that there is a close interaction between TiO$_2$ and g-C$_3$N$_4$ owing to the one-step hydrothermal reaction.

. The phase and structure of the as-prepared samples were measured by XRD, and the results were shown in Fig. S6. For pristine TiO$_2$, the diffraction peaks at 2θ values of 25.8°, 36.5°, 38.2°, 48.5°, 54.5°, 55.5° and 63.2°could be assigned to the (101), (103), (004), (200), (105), (211) and (204) crystal planes of anatase, respectively. In addition, peaks at 27.9°, 41.7°, 43.5°, 69.4°, and 70.8° were observed, which could be attributed to the (110), (111), (210), (301), and (112) crystal planes of rutile, respectively. The results confirmed that the TiO$_2$ nanoparticles possess two crystal phases, namely the anatase and rutile phases. Pure g-C$_3$N$_4$ exhibited two diffraction peaks, at 27.8°and 13.4°, corresponding to the interplanar stacked (002) crystal plane of the conjugated aromatic system and the in-plane structure (100) crystal plane of the triazine unit, respectively [63,64]. Nevertheless, the characteristic peaks of TiO$_2$ and g-C$_3$N$_4$ in the TiO$_2$@LMPET, g-C$_3$N$_4$@LMPET, and g-C$_3$N$_4$-TiO$_2$@LMPET composites were not obvious, probably due to the low content of TiO$_2$ and g-C$_3$N$_4$ in the composites. At the same time, the FT-IR and Raman analysis were carried out (Figs. S7 and S8). The results of FT-IR spectra and Raman spectra indicated that g-C$_3$N$_4$ and TiO$_2$ were successfully loaded onto the LMPET. The optical properties of the as-prepared samples were characterized by DRS. As can be seen from Fig. 4, LMPET showed absorption capacity in the ultraviolet region, which derived from the benzene ring structure in LMPET [65]; however, TiO$_2$@LMPET exhibited relatively stronger absorption in the ultraviolet region because of the efficient UV-light harvesting of TiO$_2$ [66]. Meanwhile, the absorption region of g-C$_3$N$_4$@LMPET broadened to the visible region with a red shift, which was attributed to the characteristic absorption of g-C$_3$N$_4$ at 200–450 nm [67]. For the g-C$_3$N$_4$-TiO$_2$@LMPET, the absorption edge underwent a red shift and the absorption intensity increased compared to the TiO$_2$@LMPET and g-C$_3$N$_4$@LMPET, which could be ascribed to the synergetic effect of TiO$_2$ and g-C$_3$N$_4$. These results implied that the obtained g-C$_3$N$_4$-TiO$_2$@LMPET leads to a higher utilization of light energy, which helps to improve the photocatalytic efficiency.

The thermal stability of all samples was tested by TGA. As shown in Fig. S9, there was no mass loss of TiO$_2$ in the temperature range of 25–800 °C, while the decomposition of g-C$_3$N$_4$ started at approximately 500 °C and ended at about 750 °C. The TG curve of the LMPET showed two mass-loss stages, and the final decomposition temperature of g-C$_3$N$_4$-TiO$_2$@LMPET was higher than that of LMPET, which have been
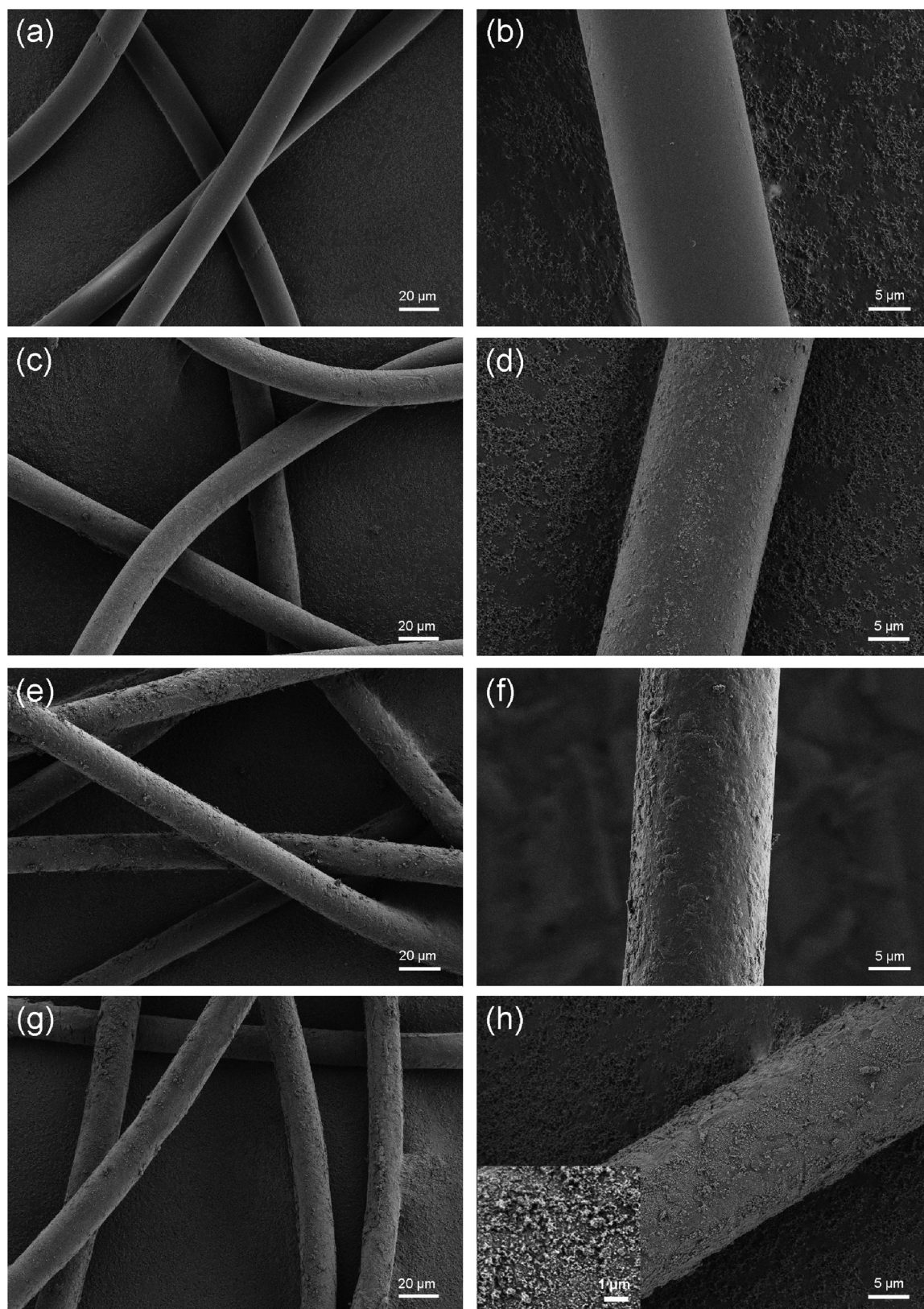
Fig. 1. SEM images of the samples. (a, b) LMPET; (c, d) TiO$_2$@LMPET; (e, f) g-C$_3$N$_4$@LMPET; (g, h) g-C$_3$N$_4$-TiO$_2$@LMPET.

due to the high melting temperature of TiO$_2$ deposited on the surface of g-C$_3$N$_4$@LMPET. Unexpectedly, the total mass loss of g-C$_3$N$_4$-TiO$_2$@LMPET was consistent with that of LMPET, close to 100%, and no TiO$_2$ remained, which could be explained by the fact that the TiO$_2$ deposited on the surface of g-C$_3$N$_4$@LMPET was removed by the air flow with the

decomposition of g-C$_3$N$_4$.

3.2. Photocatalytic activity of catalysts

The antibiotic SQX and the pesticide thiamethoxam were selected as
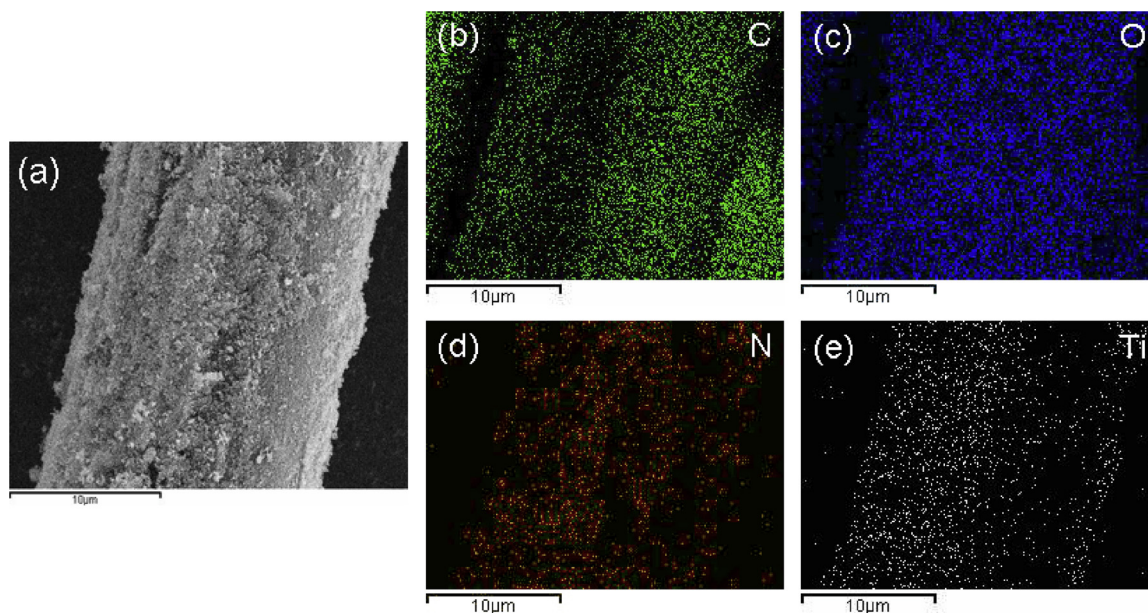
Fig. 2. (a) Morphology of the g-C$_3$N$_4$-TiO$_2$@LMPET surface; (b–e) EDX elemental mapping results of the g-C$_3$N$_4$-TiO$_2$@LMPET surface.

the two main target pollutants to study the catalytic activity of the photocatalysts, and the results are shown in Fig. 5. Meanwhile, the adsorption experiments of SQX and thiamethoxam under dark condition were carried out. As can be seen from Fig. S10, the substrates SQX and thiamethoxam were basically not adsorbed by LMPET, TiO$_2$@LMPET, g-C$_3$N$_4$@LMPET and g-C$_3$N$_4$-TiO$_2$@LMPET. The photocatalytic degradation of SQX was shown in Fig. 5a. It can be seen that the concentration of SQX was a little decreased under sunlight radiation. In the presence of TiO$_2$@LMPET or g-C$_3$N$_4$@LMPET, the removal efficiency of SQX reached nearly 40% and 50%, respectively. However, the g-C$_3$N$_4$-TiO$_2$@LMPET showed a higher photocatalytic efficiency, achieving a removal rate of over 97% within 90 min, which indicates that the g-C$_3$N$_4$-TiO$_2$@LMPET combining TiO$_2$ with g-C$_3$N$_4$, could more efficiently eliminate pollutants.

Thiamethoxazine is a harder-to-degrade contaminant and the degradation result was shown in Fig. 5b. It can be seen that thiamethazine was also slightly photodegraded under solar radiation, and g-C$_3$N$_4$-TiO$_2$@LMPET exhibited a significantly higher photocatalytic activity for the removal of thiamethoxam than TiO$_2$@LMPET and g-C$_3$N$_4$@LMPET, which was consistent with the results presented in Fig. 5a. There was no obvious change in the concentration of thiamethoxazine in the presence of g-C$_3$N$_4$@LMPET, which suggests that g-C$_3$N$_4$@LMPET had a significantly poor photocatalytic activity for the removal of thiamethoxam. Based on the above results, it can be concluded that TiO$_2$ in the g-C$_3$N$_4$-TiO$_2$@LMPET plays a main role in the degradation of toxic and stubborn contaminants. Meanwhile, the photocatalytic performance of the as-prepared photocatalysts under visible light irradiation (> 420 nm) was investigated (Fig. S11). As shown in Fig. 5, SQX and thiamethoxazine were quite stable under visible light irradiation, which implied that their own photodegradation was mainly caused by the ultraviolet irradiation in sunlight. Moreover, as can be seen from Fig. S11, TiO$_2$@LMPET had almost no catalytic activity in the degradation of substrates under visible light, and the photocatalytic activity of g-C$_3$N$_4$-TiO$_2$@LMPET was still higher than that of g-C$_3$N$_4$@LMPET, which additionally confirmed that the enhanced catalytic activity was not only due to the simple physical combination of TiO$_2$ and g-C$_3$N$_4$, but could also be attributed to the synergistic effect between TiO$_2$ and g-C$_3$N$_4$ [68]. To further investigate the interaction between g-C$_3$N$_4$ and TiO$_2$, PL was used to demonstrate the interface charge transfer behavior. As can be seen in Fig. 6, the g-C$_3$N$_4$@LMPET presented a strong emission peak around 450 nm, while the PL intensity of

g-C$_3$N$_4$-TiO$_2$@LMPET was much lower than that of g-C$_3$N$_4$@LMPET, which demonstrated that the electrons in the CB of g-C$_3$N$_4$ could be transferred to TiO$_2$ and efficiently suppress the recombination of photogenerated electron-hole pairs [69,70], in agreement with the results of XPS analysis. To further investigate the separation efficiency of photogenerated electron-hole pairs, the photocurrent-time measurements were performed. As shown in Fig. S12, g-C$_3$N$_4$/TiO$_2$ exhibited a better photocurrent density response than pure g-C$_3$N$_4$ and TiO$_2$, which suggests that the photogenerated electron–hole pairs of g-C$_3$N$_4$/TiO$_2$ can be separated efficiently.Furthermore, it was observed that the degradation trends of the substrates by TiO$_2$@LMPET and g-C$_3$N$_4$@LMPET were different from that of g-C$_3$N$_4$-TiO$_2$@LMPET. The substrate degradation by g-C$_3$N$_4$-TiO$_2$@LMPET showed a usual trend, characterized by an initial high rate of degradation, followed by a slower degradation. On the other hand, the substrate degradation by TiO$_2$@LMPET or g-C$_3$N$_4$@LMPET presented an opposite trend, and the catalytic degradation of substrates hardly occurred during the first 30 min. This phenomenon was attributed to the hydrophobicity of the samples' surface, as demonstrated using the water wettability test (Movie S1). In Movie S1, LMPET + TiO$_2$ was prepared by directly immersing LMPET into the TiO$_2$ suspension and then drying it at 60 °C. The obtained LMPET + TiO$_2$ was a hydrophilic material in which TiO$_2$ was fully exposed to the surface of LMPET, whereas TiO$_2$@LMPET was a hydrophobic material where most of the TiO$_2$ particles were wrapped into the PET fibers during the 135 °C baking treatment due to their small particle size. As can be seen in Movie S1, when water dripped on the surface of LMPET and g-C$_3$N$_4$@LMPET, nearly spherical water droplets were formed, which was attributed to the hydrophobicity of the PET fibers and g-C$_3$N$_4$. Similarly, water formed near-spherical droplets on the surface of TiO$_2$@LMPET, mainly because the TiO$_2$ wrapped into the LMPET was unable to show hydrophilicity. On the contrary, g-C$_3$N$_4$-TiO$_2$@LMPET and LMPET + TiO$_2$ were readily wetted once the water droplets fell on their surface, indicating that the hydrophilicity of LMPET could be improved by coating the surface of PET fibers with TiO$_2$ [71]. Therefore, for the TiO$_2$@LMPET and g-C$_3$N$_4$@LMPET, the removal of substrates included two processes: the first process, which is a wetting process, there was sufficient contact between the catalysts and the substrates; the second process, there was mainly photocatalytic degradation of the substrate. However, for the g-C$_3$N$_4$-TiO$_2$@LMPET, TiO$_2$ was completely exposed to the surface, resulting in superior hydrophilicity, which was conducive to the contact between the catalyst
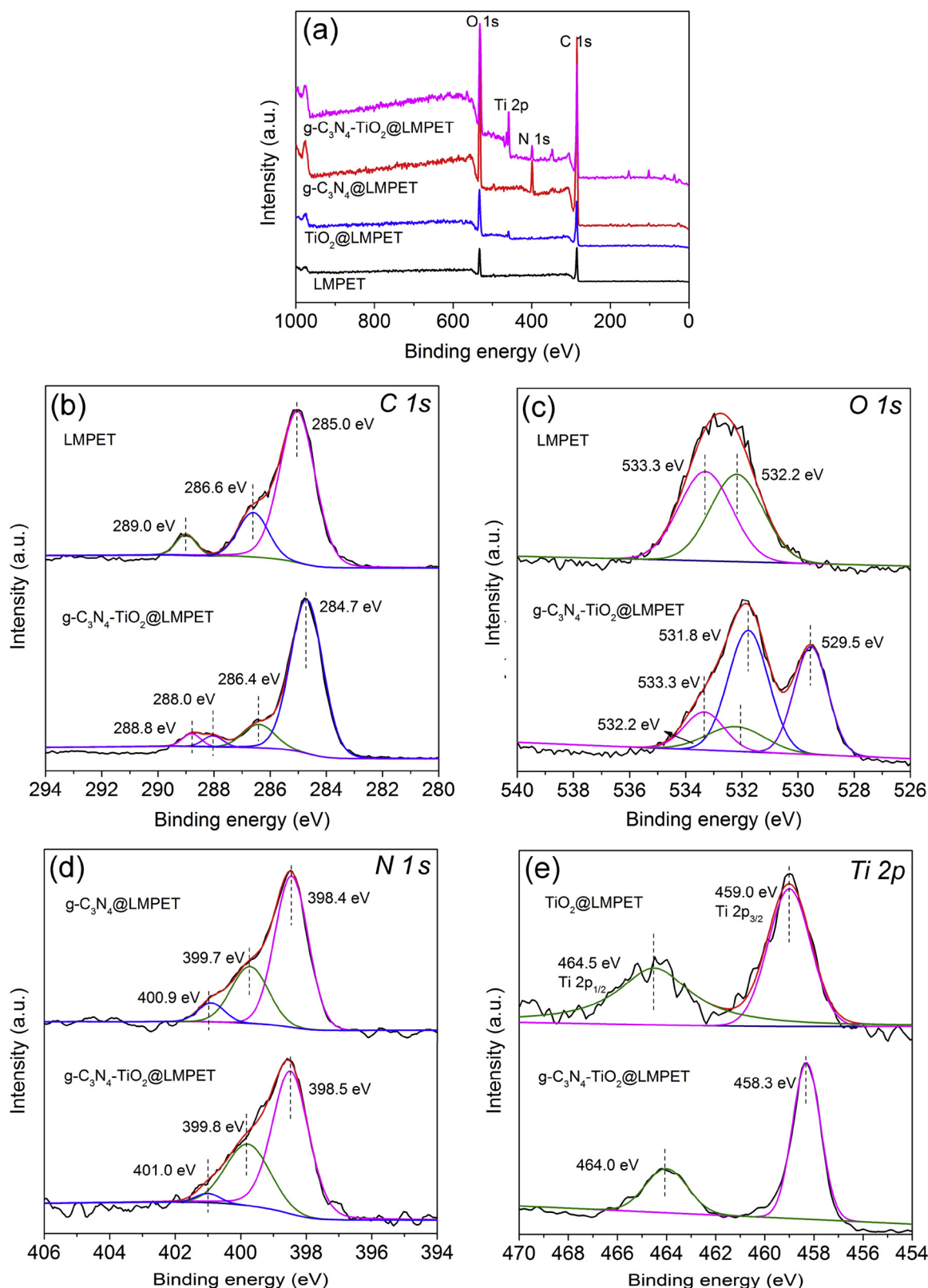
Fig. 3. Survey and high resolution XPS spectra of the samples. (a) XPS survey spectra; (b) C 1s spectra of LMPET and g-C$_3$N$_4$-TiO$_2$@LMPET; (c) O 1s spectra of LMPET and g-C$_3$N$_4$-TiO$_2$@LMPET; (d) N 1s spectra of g-C$_3$N$_4$@LMPET and g-C$_3$N$_4$-TiO$_2$@LMPET; (e) Ti 2p spectra of TiO$_2$@LMPET and g-C$_3$N$_4$-TiO$_2$@LMPET.

and the substrate in aqueous solution, thereby accelerating substrate degradation.

Recyclability is an important factor for catalyst use in practice, so cycle tests for the photocatalytic degradation of SQX and thiamethoxam were performed. As shown in Fig. 7, the removal rate still reached 97% after ten reaction cycles, which demonstrated that g-C$_3$N$_4$-TiO$_2$@LMPET was reusable and maintained high catalytic activity. In order to further evaluate the structural

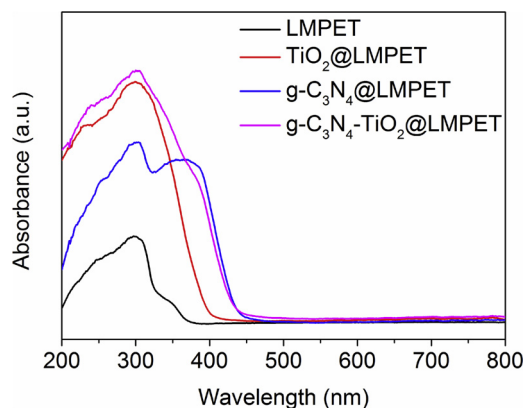**Fig. 4.** UV–vis diffuse reflectance absorption spectra of LMPET, TiO$_2$@LMPET, g-C$_3$N$_4$@LMPET and g-C$_3$N$_4$-TiO$_2$@LMPET.
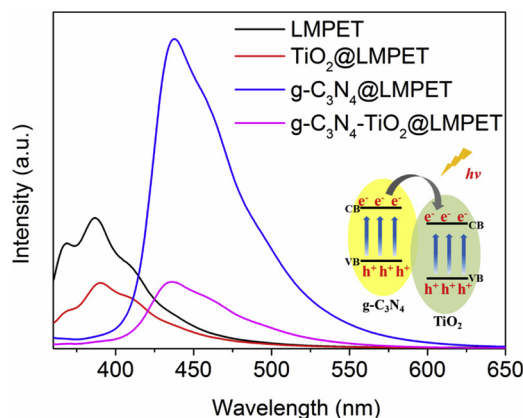
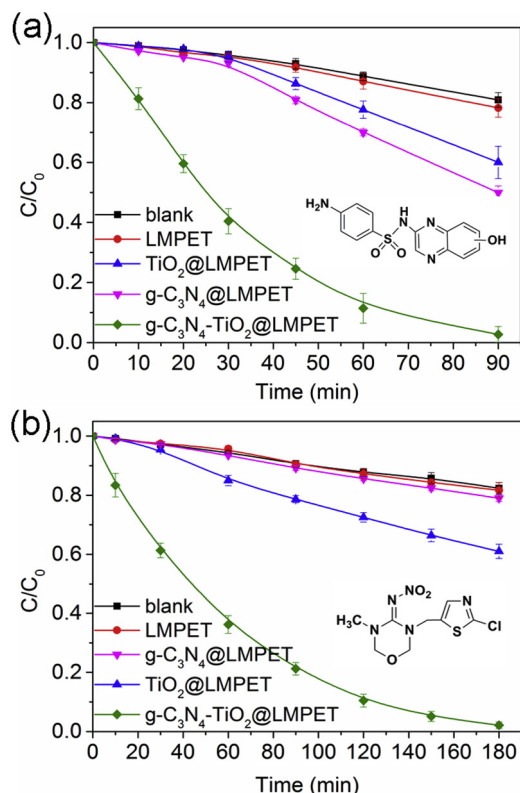**Fig. 6.** Photoluminescence (PL) spectra of LMPET, TiO$_2$@LMPET, g-C$_3$N$_4$@LMPET and g-C$_3$N$_4$-TiO$_2$@LMPET.

Fig. 5. Photocatalytic degradation of SQX (a) and thiamethoxam (b) under different conditions exposed to solar irradiation, [SQX] = 2 × 10^{-5} mol/L, [thiamethoxam] = 2 × 10^{-5} mol/L, pH 7.

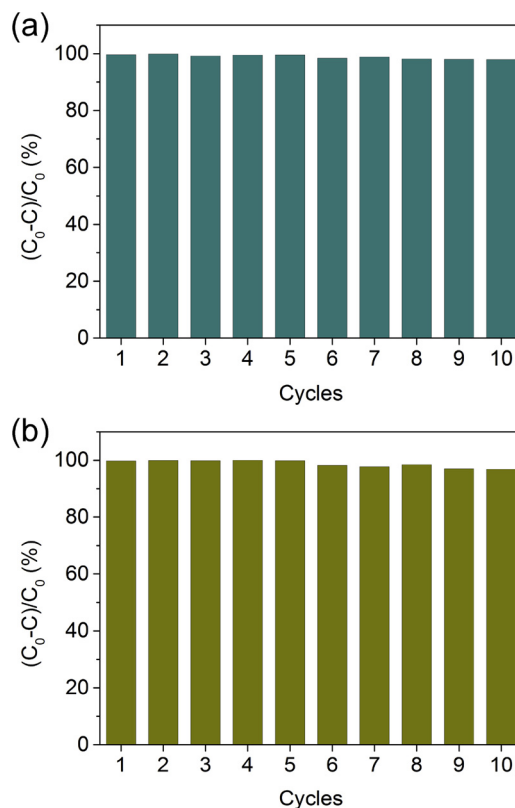**Fig. 7.** Cyclic photocatalytic degradation of SQX (a) and thiamethoxam (b) by g-C$_3$N$_4$-TiO$_2$@LMPET exposed to solar irradiation for 120 min and 210 min, respectively, [SQX] = 2 × 10^{-5} mol/L, [thiamethoxam] = 2 × 10^{-5} mol/L, pH 7.

These results suggest that the g-C$_3$N$_4$-TiO$_2$@LMPET can effectively eliminate pollutants under a wide pH range.

3.3. Stability of PET support

For supported photocatalysts, besides their activity and recyclability, the stability of the supports is another crucial issue. It is well known that PET is formed by the condensation of terephthalic acid and ethylene glycol. BHET is obtained by esterification of terephthalic acid and ethylene glycol, which can be regarded as a structural unit of polyester. Therefore, the photocatalytic degradation experiments of BHET by pure TiO$_2$ and g-C$_3$N$_4$ were carried out to estimate the effect of the immobilization of TiO$_2$ and g-C$_3$N$_4$ on the structural stability of the

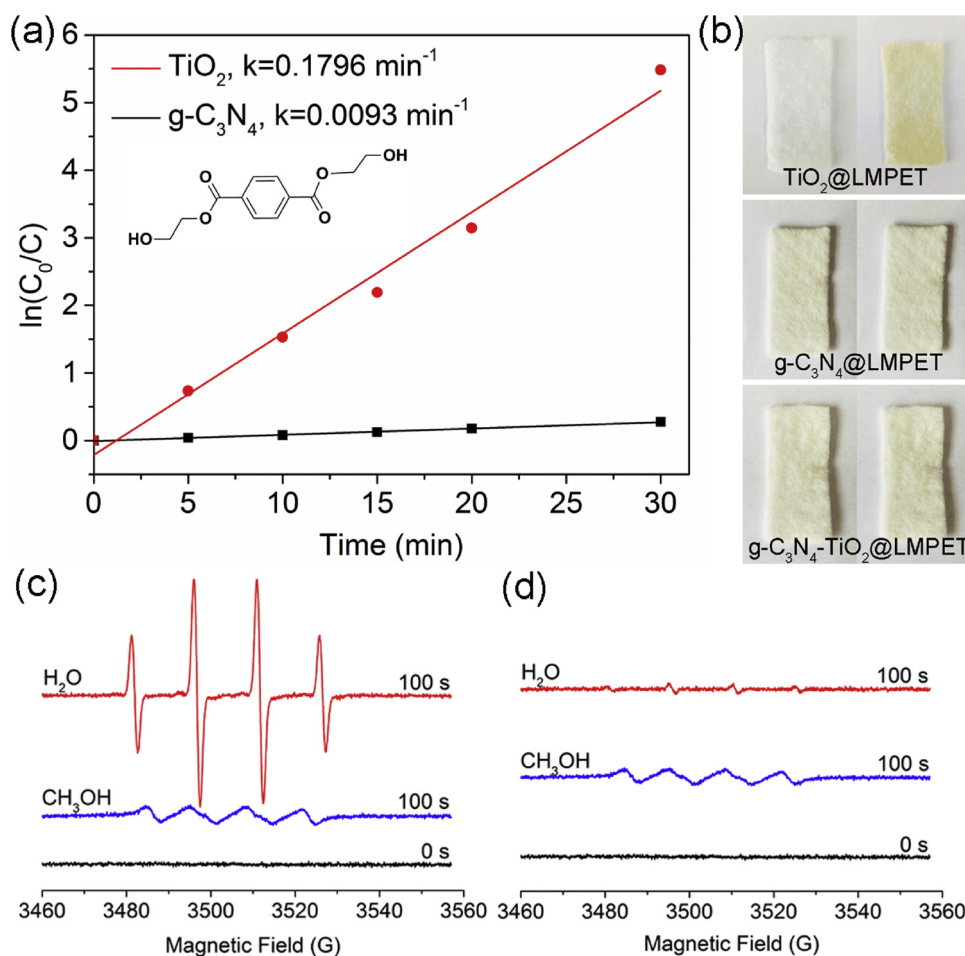stability of g-C$_3$N$_4$-TiO$_2$@LMPET, the SEM and mapping results of g-C$_3$N$_4$-TiO$_2$@LMPET after ten reaction cycles are presented in Figs. S13 and S14. The surface morphology and element distribution of g-C$_3$N$_4$-TiO$_2$@LMPET were not altered noticeably after the reaction cycles, confirming that the combination between TiO$_2$ and g-C$_3$N$_4$, as well as the bonding between g-C$_3$N$_4$ and PET fiber were firm. In addition, the photocatalytic degradation of SQX with TiO$_2$@LMPET, g-C$_3$N$_4$@LMPET, and g-C$_3$N$_4$-TiO$_2$@LMPET under different pH conditions were investigated, and the results are displayed in Fig. S15. TiO$_2$@LMPET and g-C$_3$N$_4$@LMPET exhibited higher photocatalytic activity under acidic conditions and showed lower photocatalytic activity under alkaline conditions. Nevertheless, g-C$_3$N$_4$-TiO$_2$@LMPET displayed significantly better photocatalytic performance under acidic and neutral conditions. Under alkaline conditions, the photocatalytic removal efficiency of SQX by g-C$_3$N$_4$-TiO$_2$@LMPET is twice that of TiO$_2$@LMPET.

Fig. 8. (a) Photocatalytic degradation of BHET by pure TiO$_2$ and g-C$_3$N$_4$ under solar irradiation, [BHET] = 2 × 10^{-5} mol/L, [TiO$_2$] = 0.1 g/L, [g-C$_3$N$_4$] = 0.1 g/L, pH 7; (b) Photos of the samples before and after UV light irradiation for 14 h; (c, d) DMPO spin-trapping EPR spectra in the presence of TiO$_2$ and g-C$_3$N$_4$, respectively, under solar irradiation, [DMPO] = 10 mM, pH 7.

PET fibers under solar irradiation. The degradation efficiency of BHET was quantified according to a pseudo-first-order kinetic model, ln(C$_0$/C) = kt (Fig. 8a), where C$_0$ and C represent concentrations at time 0 and t, respectively. Based on the fitting results, the rate constant (k) of BHET degradation with TiO$_2$ (0.1793 min^{-1}) was about 19 times higher than that of g-C$_3$N$_4$ (0.0093 min^{-1}), which suggests that TiO$_2$ can destroy the structure of BHET under solar irradiation, but g-C$_3$N$_4$ was almost completely ineffective. It was inferred that the main chain of PET could be broken by TiO$_2$ when exposed to sunlight.

In order to further study the mechanism of photo-etching of PET fibers induced by TiO$_2$, an electron paramagnetic resonance (EPR) technology (with DMPO) was used (Fig. 8c and d). The results of the EPR analysis indicated that the main active species generated by TiO$_2$ in the TiO$_2$/sunlight system was ˙OH, while the dominating active species for the g-C$_3$N$_4$/sunlight system was ˙O$_2^-$. It is worth noting that ˙OH, with strong oxidative activity, is very active and non-selective [72], were as the oxidation reaction of ˙O$_2^-$ is selective. Therefore, we can infer that under the excitation of sunlight, ˙OH formed on the surface of TiO$_2$ attacked the main chain structure of PET, accelerating the photo-oxidation of PET fibers, while ˙O$_2^-$ was inactive for cleaving the main PET chain.

The UV irradiation tests of the as-prepared samples intuitively proved the conclusion that the immobilization of TiO$_2$ onto the PET fibers could accelerate the photo-oxidation of PET. Photos of these samples before and after UV exposure were shown in Figs. 8b and S16. As can be seen in Fig. S16, no change was observed in pristine LMPET after 14 h of UV light exposure. However, Fig. 8b showed that the high-

intensity UV irradiation caused a significant change in the color of the TiO$_2$@LMPET, from white to yellow. This phenomenon could be explained by the fact that ˙OH produced by TiO$_2$ attacks the aromatic groups of PET to produce dihydroxy compounds, resulting in the formation of quinoid structures that are responsible for the change in color [73]. As expected, there were no visible changes in the g-C$_3$N$_4$@LMPET and g-C$_3$N$_4$-TiO$_2$@LMPET after 14 h exposure to UV light, and their color was light yellow, which originated from the color of pure g-C$_3$N$_4$. The results showed that the PET support could be shielded by the g-C$_3$N$_4$ coating from the attack of ˙OH, thus g-C$_3$N$_4$-TiO$_2$@LMPET had a better stability than TiO$_2$@LMPET under solar irradiation.

3.4. Mechanisms and pathways of degradation

DMPO spin-trapping EPR was used to examine the active species generated by g-C$_3$N$_4$-TiO$_2$@LMPET during the photocatalytic process. As shown in Fig. 9a, the DMPO-˙OH and DMPO-˙O$_2^-$ signals were significantly detected in the aqueous and methanol solution, respectively, indicating that ˙OH and ˙O$_2^-$ were generated in the g-C$_3$N$_4$-TiO$_2$@LMPET catalytic system. Meanwhile, the EPR analysis of TiO$_2$@LMPET was performed, and the result was displayed in Fig. S17. Compared to the EPR results of pure TiO$_2$, the DMPO-˙OH signal of TiO$_2$@LMPET was very weak. A possible reason for this was that part of the supported TiO$_2$ nanoparticles were wrapped into the PET fibers during the 135 °C heat-baking treatment, resulting in the detection of weaker EPR signals. Therefore, it can be inferred from the EPR results of g-C$_3$N$_4$-TiO$_2$@LMPET that TiO$_2$ was successfully deposited on the
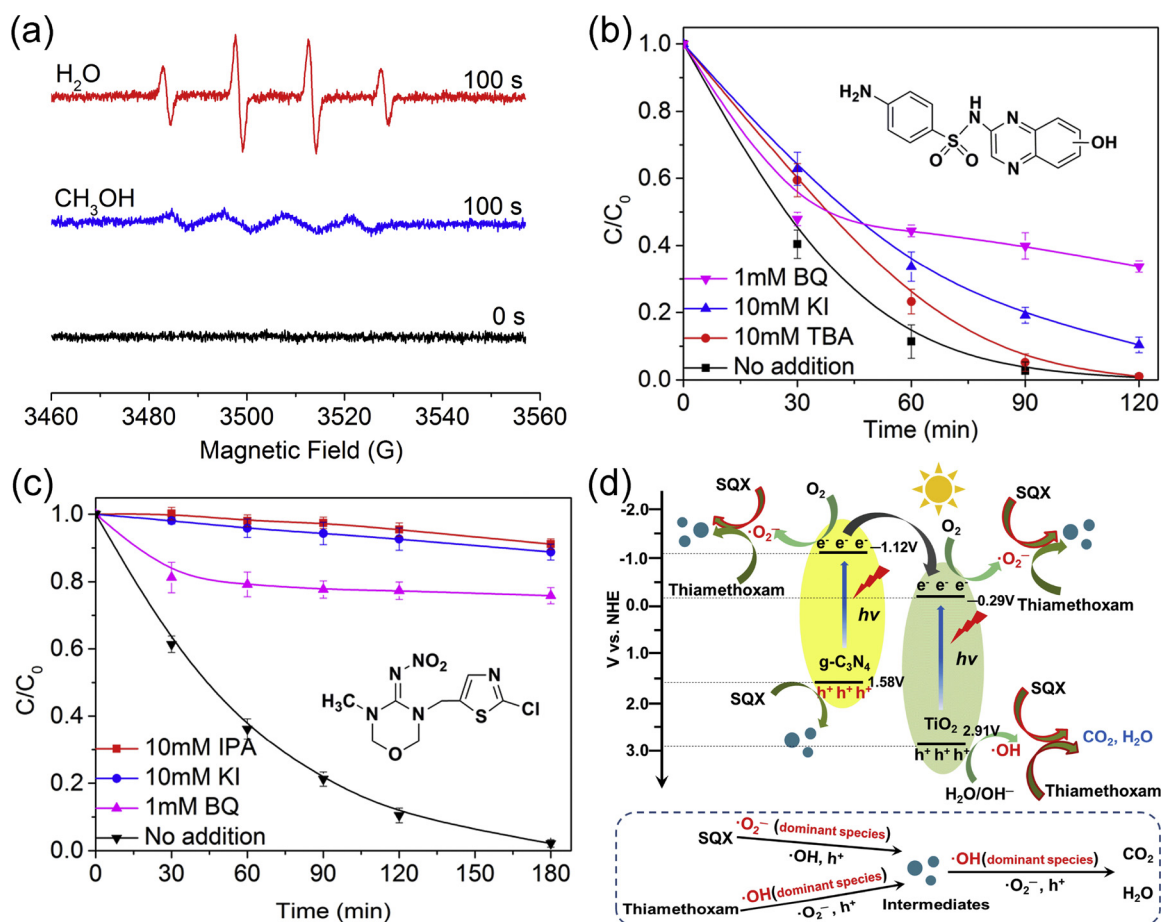
Fig. 9. (a) DMPO spin-trapping EPR spectra in aqueous or methyl alcohol solutions in the presence of g-C_3N_4-TiO_2@LMPET under solar irradiation, [DMPO] = 10 mM; (b, c) Effect of trapping agents on photocatalytic degradation of SQX and thiamethoxam, respectively, by g-C_3N_4-TiO_2@LMPET under solar irradiation, [SQX] = 2×10^{-5} mol/L, [thiamethoxam] = 2×10^{-5} mol/L, pH 7; (d) Possible photocatalytic mechanism for g-C_3N_4-TiO_2@LMPET under solar irradiation.

surface of g-C_3N_4@LMPET, and the TiO_2 active sites were sufficiently exposed, contributing to the degradation reaction of substrates.

To further investigate the dominant active species in the degradation of SQX and thiamethoxam by g-C_3N_4-TiO_2@LMPET, classical quenching tests were performed, and the results were shown in Fig. 9b and c. The scavengers, TBA or IPA, KI, and BQ were used to quench the active species: ·OH, hole (h$^+$), and ·O_2^-, respectively. The result presented in Fig. 9b suggests that ·O_2^-, h$^+$, and ·OH were present in the g-C_3N_4-TiO_2@LMPET/sunlight catalytic system and ·O_2^- played a major role in the removal of SQX. As can be seen in Fig. 9c, the thiamethoxam removal rate declined noticeably in the presence of IPA, KI, and BQ. The inhibition effect was strongest in the presence of IPA, followed by KI. Notably, KI can trap h$^+$ and hinder the formation of ·OH, thus leading to a significant decrease in the degradation rate of thiamethoxam. Therefore, we deduced that ·OH was the dominant species for the degradation of thiamethoxam with g-C_3N_4-TiO_2@LMPET, accompanied by the formation of ·O_2^-. According to the above results, it can be concluded that the three active species ·O_2^-, ·OH and h$^+$, worked together to efficiently remove the target pollutants, SQX and thiamethoxam. Meanwhile, the quenching tests of g-C_3N_4@LMPET and TiO_2@LMPET were also performed, and the results were shown in Figs. S18 and S19. As can be seen from Fig. S18, ·O_2^- and ·OH were the dominant species for the degradation of SQX by TiO_2@LMPET, as well as h$^+$, ·OH and ·O_2^- worked together to remove thiamethoxam in the present of TiO_2@LMPET. As can be seen from Fig. S19, ·O_2^- and h$^+$ were the main active species for the removal of SQX and thiamethoxam in the present of g-C_3N_4@LMPET. Subsequently, a plausible

photocatalytic mechanism for g-C_3N_4-TiO_2@LMPET was proposed. As shown in Fig. 9d, g-C_3N_4 and TiO_2 were simultaneously excited by solar light to generate electron-hole pairs. The photogenerated electrons on the CB of g-C_3N_4 could react with dissolved oxygen to form ·O_2^- species that mainly oxidized SQX into intermediates, the electrons could then be further transferred to the CB of TiO_2. At the same time, the holes formed on g-C_3N_4 also participated in the oxidation process of SQX. On the other hand, the photogenerated holes on the VB of TiO_2 could react with H_2O or OH^- to form ·OH, which resulted in further oxidation of the SQX intermediates and direct oxidation of thiamethoxam into CO_2 and H_2O.

The degradation intermediates of SQX in the presence of g-C_3N_4-TiO_2@LMPET were examined by UPLC Synapt G2-S HDMS in both the positive and negative ion mode. The two possible degradation pathways (A, B) of SQX were shown in Fig. 10 and the details of the intermediate products were listed in Table S3. According to pathway A, SQX was first subjected to hydroxylation [74], forming the hydroxylated intermediate, P_1. Secondly, the S−C and S−N bonds were destroyed to extrude SO_2, leading to the formation of intermediate P_3. Thirdly, the formation of the P_3 intermediate was followed by the destruction of the C−N bond and the loss of the aniline group, which resulted in the generation of the P_4 intermediate. Finally, intermediate P_4 was further oxidized to intermediate P_5. Pathway B was initiated by extruding SO_2 from sulfonamides to form intermediate P_2 [75], which was then further oxidized by elimination of the aniline group to form intermediate P_6. At the end of the reaction, no small molecule acids were detected, so we inferred that the intermediate products were eventually mineralized
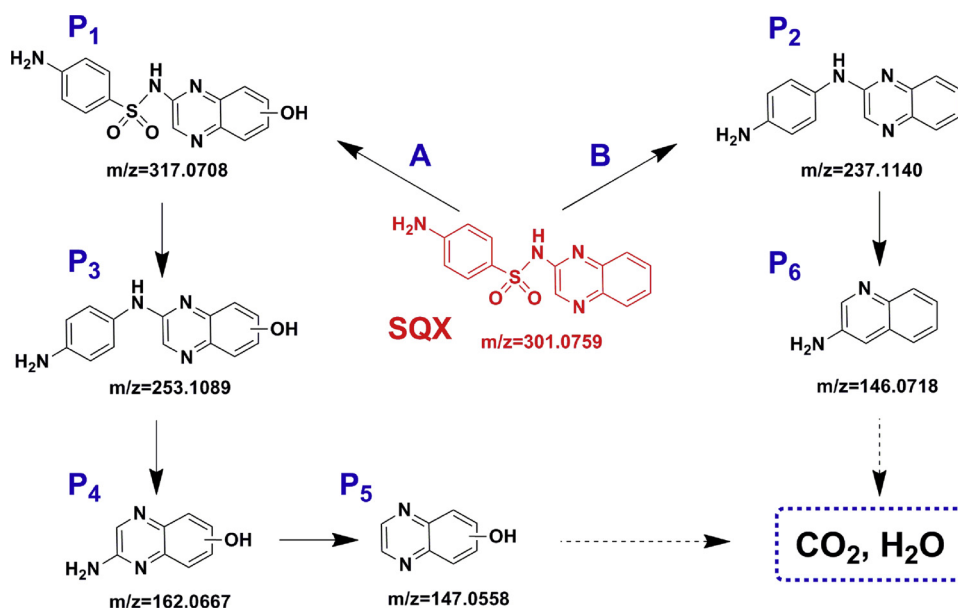
Fig. 10. Proposed possible degradation pathway of SQX by g-C_3N_4-TiO_2@LMPET under solar irradiation, pH 7.
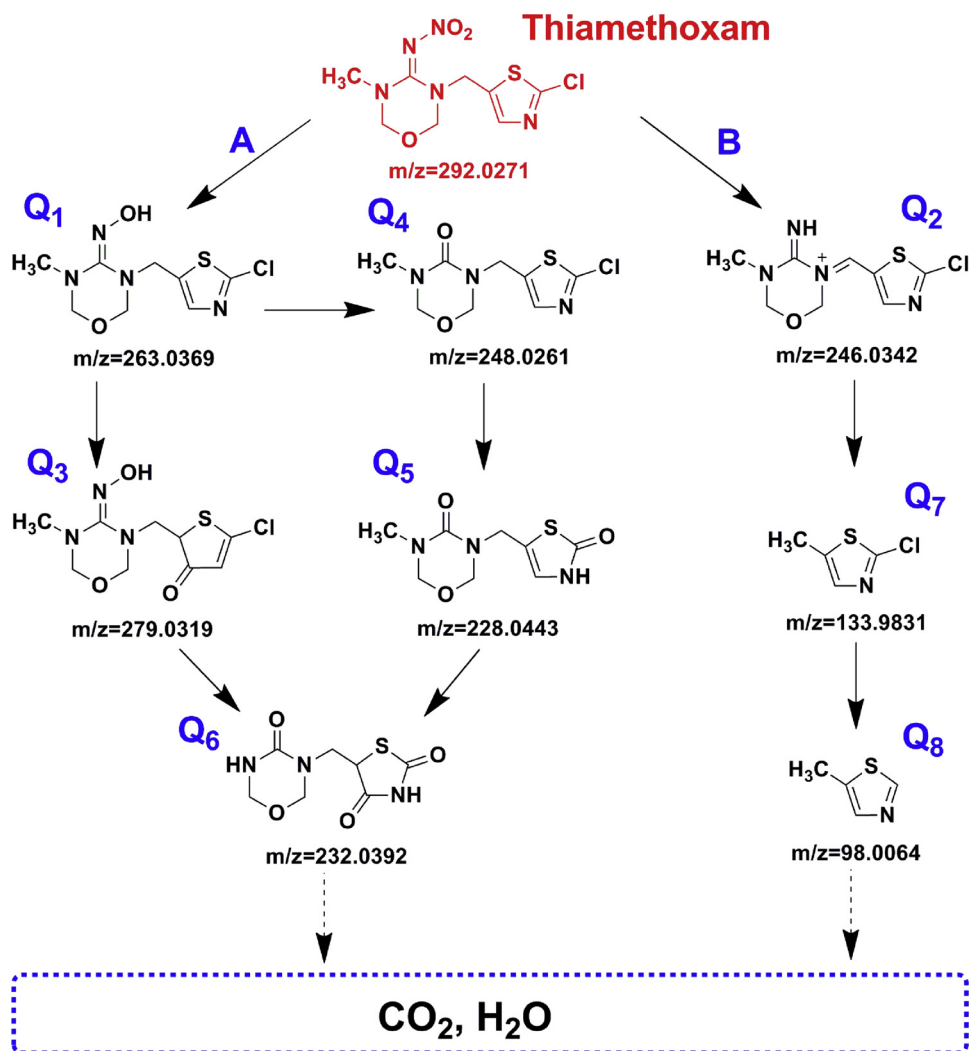

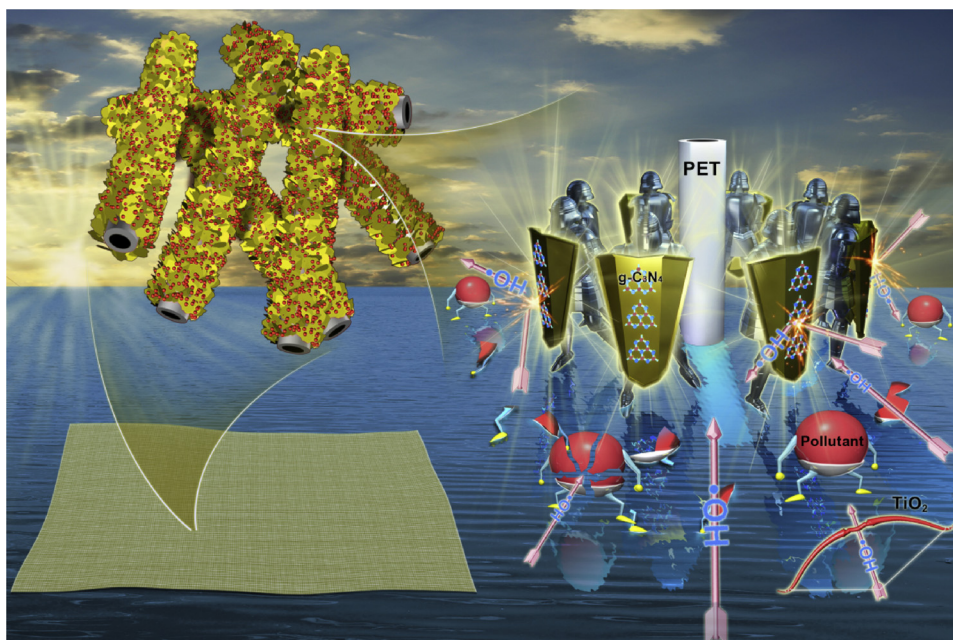**Fig. 11.** Proposed possible degradation pathway of thiamethoxam by g-C_3N_4-TiO_2@LMPET under solar irradiation, pH 7.

Fig. 12. Schematic diagram of the g-C_3N_4-shielding PET/TiO_2 composite for the removal of pollutants from water.

into CO_2 and H_2O. However, in our previous work, a series of small molecular acids were detected at the end of SQX degradation in the g-C_3N_4 catalytic system with $\cdot O_2^-$ as the main active species [76,77], confirming that $\cdot OH$ generated by the introduction of TiO_2 into g-C_3N_4-TiO_2@LMPET has a stronger oxidizing ability and could further oxidize the produced intermediates into CO_2 and H_2O, in agreement with the catalytic mechanism proposed above.

The detected degradation intermediates of thiamethoxam were listed in Table S4. Considering the results of the above photocatalytic degradation experiments, we inferred that $\cdot OH$ was mainly responsible for the oxidation of thiamethoxam with g-C_3N_4-TiO_2@LMPET. Therefore, two plausible degradation pathways were proposed, as shown in Fig. 11. In pathway A, the nitro group of thiamethoxam was replaced by a hydroxyl group to form the intermediate Q_1 [78]. Further oxidation occurred in the thiazole and 1,3,5-oxadiazinane rings to generate the intermediates Q_3 and Q_4, respectively. Subsequently, the chlorine group in intermediate Q_4 was attacked by the hydroxyl radical, yielding the intermediate Q_5 [79]. The intermediates Q_3 and Q_5 were further oxidized to the intermediate Q_6. In pathway B, thiamethoxam lost a nitro group and a hydrogen atom from the methylene group, which connected to the 1,3,5-oxadiazolidine and the thiazole rings, resulting in the formation of the intermediate Q_2. The methine group between the 1,3,5-oxadiazolidine ring and the thiazole ring was then cleaved to form the fragmentation product, Q_7. After that, the loss of the chlorine group took place in the intermediate Q_7 to obtain Q_8. Eventually, all intermediates could be mineralized into inorganic substances, namely carbon dioxide and water. Based on these results, it was deduced that for stubborn contaminants, such as thiamethoxam with an electron-withdrawing nitro group and a chlorine group, the $\cdot O_2^-$ generated by g-C_3N_4 is difficult to attack and destroy the structure, while $\cdot OH$ generated by TiO_2 with stronger oxidizing ability can make thiamethoxazine undergo the dechlorination and denitrification reactions, and further mineralization [80,81]. As shown in Fig. 12, in the flexible g-C_3N_4-TiO_2@LMPET fiber mat floating on the water, TiO_2 exhibits major contribution to the elimination of recalcitrant pollutants, and the g-C_3N_4 layer acts as an "armor" to protect PET from damage by $\cdot OH$ generated by TiO_2.

4. Conclusion

The g-C_3N_4-TiO_2@LMPET composite has been successfully prepared through a facile method. Compared with the TiO_2@LMPET and g-C_3N_4@LMPET, the g-C_3N_4-TiO_2@LMPET has a higher photocatalytic efficiency for the degradation of SQX and thiamethoxam under solar irradiation, which can be ascribed to extended light absorption, electron transfer between g-C_3N_4 and TiO_2, as well as a greater number of active sites. Meanwhile, the g-C_3N_4-TiO_2@LMPET exhibited good repeatability in cyclic experiments. Significantly, a series of tests showed that the g-C_3N_4 layer effectively avoided the damage of PET by $\cdot OH$ radicals. The trapping experiments suggested that $\cdot OH$, $\cdot O_2^-$ and h^+ were the main active species for pollutant degradation, and $\cdot OH$ led to the deep oxidation of SQX and thiamethoxam. This work provides new insights in the design of sustainable supported photocatalysts, which are expected to be applied for environmental treatment and energy conversion.

Author contributions

The manuscript was written through contributions of all authors. All authors have given approval to the final version of the manuscript.

Acknowledgments

Appendix A. Supplementary data

Supplementary material related to this article can be found, in the online version, at doi:https://doi.org/10.1016/j.apcatb.2019.117960.

References

[1] H. Xie, X. Wang, J. Chen, X. Li, G. Jia, Y. Zou, Y. Zhang, Y. Cui, Sci. Total Environ. 656 (2019) 946–951.

[2] R. Karmakar, G. Kulshrestha, Pest Manage. Sci. 65 (2009) 931–937.

[3] S. Ahmed, M.G. Rasul, R. Brown, M.A. Hashib, J. Environ. Manage. 92 (2011) 311–330.

[4] C.K. Myresiotis, Z. Vryzas, E. Papadopoulou-Mourkidou, Biodegradation 23 (2012) 297–310.

[5] B. Pan, W. Du, W. Zhang, X. Zhang, Q. Zhang, B. Pan, L. Lv, Q. Zhang, J. Chen, Environ. Sci. Technol. 41 (2007) 5057–5062.

[6] H. Wang, W. Jiang, Ind. Eng. Chem. Res. 46 (2007) 5405–5411.

[7] L. Feng, G. Yang, L. Zhu, X. Xu, F. Gao, J. Mu, Y. Xu, Bioresour. Technol. 187 (2015) 331–337.

[8] S. Gartiser, E. Urich, R. Alexy, K. Kummerer, Chemosphere 67 (2007) 604–613.

[9] Y. Wang, Y. Liu, T. Liu, S. Song, X. Gui, H. Liu, P. Tsiakaras, Appl. Catal. B 156–157 (2014) 1–7.

[10] A.Y. Lin, C.F. Lin, J.M. Chiou, P.K. Hong, J. Hazard. Mater. 171 (2009) 452–458.

[11] A. Dirany, I. Sires, N. Oturan, A. Ozcan, M.A. Oturan, Environ. Sci. Technol. 46 (2012) 4074–4082.

[12] J. Zhao, N. Li, R. Yu, Z. Zhao, J. Nan, Chem. Eng. J. 349 (2018) 530–538.

[13] H. Zhao, S. Chen, X. Quan, H. Yu, H. Zhao, Appl. Catal. B 194 (2016) 134–140.

[14] R. Molinari, P. Argurio, Water Res. 109 (2017) 327–336.

[15] S.H. Joo, J.Y. Park, C.K. Tsung, Y. Yamada, P.D. Yang, G.A. Somorjai, Nat. Mater. 8 (2009) 126–131.

[16] D. Liu, G. Li, J. Liu, Y. Wei, H. Guo, ACS Appl. Mater. Interfaces 10 (2018) 22119–22129.

[17] L. Meng, X. Zhu, E.J.M. Hensen, ACS Catal. 7 (2017) 2709–2719.

[18] H. Watanabe, S. Asano, S.-i. Fujita, H. Yoshida, M. Arai, ACS Catal. 5 (2015) 2886–2894.

[19] A. Barroso-Bogeat, M. Alexandre-Franco, C. Fernández-González, A. Macías-García, V. Gómez-Serrano, Ind. Eng. Chem. Res. 55 (2016) 5200–5206.

[20] B. Erjavec, P. Hudoklin, K. Perc, T. Tišler, M.S. Dolenc, A. Pintar, Appl. Catal. B 183 (2016) 149–158.

[21] A. Elhage, B. Wang, N. Marina, M.L. Marin, M. Cruz, A.E. Lanterna, J.C. Scaiano, Chem. Sci. 9 (2018) 6844–6852.

[22] M.-S. Cao, W.-L. Song, Z.-L. Hou, B. Wen, J. Yuan, Carbon 48 (2010) 788–796.

[23] X. Zhang, X. Fan, C. Yan, H. Li, Y. Zhu, X. Li, L. Yu, ACS Appl. Mater. Interfaces 4 (2012) 1543–1552.

[24] F. Ali, S.B. Khan, T. Kamal, K.A. Alamry, A.M. Asiri, T.R.A. Sobahi, Sci. Rep. 7 (2017) 16957.

[25] F. Sarker, N. Karim, S. Afroj, V. Koncherry, K.S. Novoselov, P. Potluri, ACS Appl. Mater. Interfaces 10 (2018) 34502–34512.

[26] J. Fu, B. Zhu, W. You, M. Jaroniec, J. Yu, Appl. Catal. B 220 (2018) 148–160.

[27] Z. Zhou, W. Lu, N. Li, T. Xu, W. Chen, Chem. Eng. J. 321 (2017) 58–66.

[28] B.A. Patterson, H.A. Sodano, ACS Appl. Mater. Interfaces 8 (2016) 33963–33971.

[29] S. Horikoshi, N. Serpone, Y. Hisamatsu, H. Hidaka, Environ. Sci. Technol. 32 (1998) 4010–4016.

[30] H. Hidaka, Y. Suzuki, K. Nohara, S. Horikoshi, Y. Hisamatsu, E. Pelizzetti, N. Serpone, J. Polym. Sci. Part A: Polym. Chem. 34 (1996) 1311–1316.

[31] X.F. Yao, D.L. Liu, H.Y. Yeh, J. Appl. Polym. Sci. 106 (2007) 3253–3258.

[32] C. Chen, W. Ma, J. Zhao, Chem. Soc. Rev. 39 (2010) 4206–4219.

[33] Q. Xiang, J. Yu, M. Jaroniec, Nanoscale 3 (2011) 3670–3678.

[34] W. Lu, T. Xu, Y. Wang, H. Hu, N. Li, X. Jiang, W. Chen, Appl. Catal. B 180 (2016) 20–28.

[35] H. Jia, D. Ma, S. Zhong, L. Li, L. Li, L. Xu, B. Li, Chem. Eng. J. 368 (2019) 165–174.

[36] X. Wang, S. Blechert, M. Antonietti, ACS Catal. 2 (2012) 1596–1606.

[37] W.J. Ong, L.L. Tan, Y.H. Ng, S.T. Yong, S.P. Chai, Chem. Rev. 116 (2016) 7159–7329.

[38] X. Guo, X. Li, L. Qin, S.-Z. Kang, G. Li, Appl. Catal. B 243 (2019) 1–9.

[39] X. Wang, F. Wang, C. Bo, K. Cheng, J. Wang, J. Zhang, H. Song, Appl. Surf. Sci. 453 (2018) 320–329.

[40] P. Wang, Y. Mao, L. Li, Z. Shen, X. Luo, K. Wu, P. An, H. Wang, L. Su, Y. Li, S. Zhan, Angew. Chem. Int. Ed. (2019), https://doi.org/10.1002/anie.201904571.

[41] P. Wang, S. Zhan, Y. Xia, S. Ma, Q. Zhou, Y. Li, Appl. Catal. B 207 (2017) 335–346.

[42] J. Cai, Z.A. Huang, K. Lv, J. Sun, K. Deng, RSC Adv. 4 (2014) 19588–19593.

[43] L. Zhao, X. Chen, X. Wang, Y. Zhang, W. Wei, Y. Sun, M. Antonietti, M.M. Titirici, Adv. Mater. 22 (2010) 3317–3321.

[44] X. Wang, X. Chen, A. Thomas, X. Fu, M. Antonietti, Adv. Mater. 21 (2009) 1609–1612.

[45] X. Liu, J. Iocozzia, Y. Wang, X. Cui, Y. Chen, S. Zhao, Z. Li, Z. Lin, Energy Environ. Sci. 10 (2017) 402–434.

[46] C. Xie, J. Song, H. Wu, Y. Hu, H. Liu, Z. Zhang, P. Zhang, B. Chen, B. Han, J. Am. Chem. Soc. 141 (2019) 4002–4009.

[47] X. Song, Y. Hu, M. Zheng, C. Wei, Appl. Catal. B 182 (2016) 587–597.

[48] Y. Tan, Z. Shu, J. Zhou, T. Li, W. Wang, Z. Zhao, Appl. Catal. B 230 (2018) 260–268.

[49] L. Zhang, D. Jing, X. She, H. Liu, D. Yang, Y. Lu, J. Li, Z. Zheng, L. Guo, J. Mater. Chem. A 2 (2014) 2071–2078.

[50] X. Wang, W. Lu, Y. Chen, N. Li, Z. Zhu, G. Wang, W. Chen, Chem. Eng. J. 335 (2018) 82–93.

[51] P.A. Sreekumar, K. Joseph, G. Unnikrishnan, S. Thomas, Compos. Sci. Technol. 67 (2007) 453–461.

[52] M. Ramesh, K. Palanikumar, K.H. Reddy, Compos. Part B 48 (2013) 1–9.

[53] F. Dong, L. Wu, Y. Sun, M. Fu, Z. Wu, S.C. Lee, J. Mater. Chem. 21 (2011) 15171.

[54] X.-j. Wang, W.-y. Yang, F.-t. Li, Y.-b. Xue, R.-h. Liu, Y.-j. Hao, Ind. Eng. Chem. Res. 52 (2013) 17140–17150.

[55] R. Hao, G. Wang, H. Tang, L. Sun, C. Xu, D. Han, Appl. Catal. B 187 (2016) 47–58.

[56] J. Zou, J. Gao, Y. Wang, J. Photochem. Photobiol. A: Chem. 202 (2009) 128–135.

[57] J. Kim, D. Monllor-Satoca, W. Choi, Energy Environ. Sci. 5 (2012) 7647.

[58] F. Raziq, Y. Qu, M. Humayun, A. Zada, H. Yu, L. Jing, Appl. Catal. B 201 (2017) 486–494.

[59] S.J. Yang, J.H. Cho, G.H. Oh, K.S. Nahm, C.R. Park, Carbon 47 (2009) 1585–1591.

[60] K. Sridharan, E. Jang, T.J. Park, Appl. Catal. B 142–143 (2013) 718–728.

[61] X. Wei, C. Shao, X. Li, N. Lu, K. Wang, Z. Zhang, Y. Liu, Nanoscale 8 (2016) 11034–11043.

[62] J. Ma, X. Tan, T. Yu, X. Li, Int. J. Hydrogen Energy 41 (2016) 3877–3887.

[63] S. Zhou, Y. Liu, J. Li, Y. Wang, G. Jiang, Z. Zhao, D. Wang, A. Duan, J. Liu, Y. Wei, Appl. Catal. B 158–159 (2014) 20–29.

[64] G. Liao, S. Chen, X. Quan, H. Yu, H. Zhao, J. Mater. Chem. 22 (2012) 2721–2726.

[65] H. Zhang, J.-Y. Song, C.-K. Liu, Ind. Eng. Chem. Res. 52 (2013) 7403–7412.

[66] H. Zhang, X. Lv, Y. Li, Y. Wang, J. Li, ACS Nano 4 (2010) 380–386.

[67] Y. Chen, W. Huang, D. He, Y. Situ, H. Huang, ACS Appl. Mater. Interfaces 6 (2014) 14405–14414.

[68] F. Raziq, C. Li, M. Humayun, Y. Qu, A. Zada, H. Yu, L. Jing, Mater. Res. Bull. 70 (2015) 494–499.

[69] X. Zhou, B. Jin, L. Li, F. Peng, H. Wang, H. Yu, Y. Fang, J. Mater. Chem. 22 (2012) 17900.

[70] X. Yan, Q. Gao, J. Qin, X. Hui, Z. Ye, J. Li, Z. Ma, Mater. Lett. 217 (2018) 1–4.

[71] T. Kobayashi, S. Konishi, Surf. Coat. Technol. 363 (2019) 80–86.

[72] C. Indermühle, E. Puzenat, F. Simonet, L. Peruchon, C. Brochier, C. Guillard, Appl. Catal. B 182 (2016) 229–235.

[73] W. Romão, M.F. Franco, Y.E. Corilo, M.N. Eberlin, M.A.S. Spinacé, M.-A. De Paoli, Polym. Degrad. Stab. 94 (2009) 1849–1859.

[74] Q.-N. Liao, F. Ji, J.-C. Li, X. Zhan, Z.-H. Hu, Chem. Eng. J. 284 (2016) 494–502.

[75] L. Ge, J. Chen, X. Wei, S. Zhang, X. Qiao, X. Cai, Q. Xie, Environ. Sci. Technol. 44 (2010) 2400–2405.

[76] D. Qin, W. Lu, X. Wang, N. Li, X. Chen, Z. Zhu, W. Chen, ACS Appl. Mater. Interfaces 8 (2016) 25962–25970.

[77] S. Chen, W. Lu, J. Han, H. Zhong, T. Xu, G. Wang, W. Chen, Chem. Eng. J. 359 (2019) 119–129.

[78] Y. Liu, H. Liu, Y. Li, Appl. Catal. B 84 (2008) 297–302.

[79] N.A. Mir, A. Khan, M. Muneer, S. Vijayalakhsmi, Sci. Total Environ. 458–460 (2013) 388–398.

[80] J. Meijide, J. Gómez, M. Pazos, M.A. Sanromán, J. Hazard. Mater. 319 (2016) 43–50.

[81] Y. Yao, C. Huang, Y. Yang, M. Li, B. Ren, Chem. Eng. J. 350 (2018) 960–970.